Journal of Nuclear Materials 523 (2019) 135–142

Contents lists available at ScienceDirect

Journal of Nuclear Materials

journal homepage: www.elsevier.com/locate/jnucmat

Bulk moduli and high pressure crystal structure of U_3Si_2

HPSTAR 800-2019

Xiaofeng Guo [a, b, *], Xujie Lü [c], Joshua T. White [d], Chris J. Benmore [e], Andrew T. Nelson [d, f], Robert C. Roback [b], Hongwu Xu [b, **]

[a] Department of Chemistry and Alexandra Navrotsky Institute for Experimental Thermodynamics, Washington State University, Pullman, WA, 99164, United States
[b] Earth and Environmental Sciences Division, Los Alamos National Laboratory, Los Alamos, NM, 87545, United States
[c] Center for High Pressure Science & Technology Advanced Research, Shanghai, 201203, China
[d] Materials Science and Technology Division, Los Alamos National Laboratory, Los Alamos, NM, 87545, United States
[e] Advanced Photon Source, Argonne National Laboratory, Argonne, Illinois, 60439, United States
[f] Fusion and Materials for Nuclear Systems Division, Oak Ridge National Laboratory, Oak Ridge, TN, 37830, United States

HIGHLIGHTS

- The high-pressure crystal structure of U_3Si_2 was studied by *in situ* synchrotron X-ray diffraction coupled with diamond anvil cell technique.
- The bulk modulus, determined by fitting the cell volume data to the Birch-Murnaghan equation of state, was found to be 107.11 ± 5.65 GPa.

ARTICLE INFO

Article history:
Received 7 April 2019
Received in revised form
2 June 2019
Accepted 2 June 2019
Available online 4 June 2019

Keywords:
Uranium silicide
Bulk modulus
High pressure
Synchrotron X-ray diffraction
Diamond anvil cell

ABSTRACT

Bulk moduli are important parameters to assess the mechanical performance of materials including nuclear fuels. However, little experimental data exist for U_3Si_2, a potential accident-tolerant nuclear fuel, whose bulk modulus has only been measured by resonant ultrasonic spectroscopy (RUS). In addition, the knowledge for high-pressure structural behavior and phase equilibrium of U_3Si_2 is largely lacking. Here we studied pressure dependence of the crystal structure of U_3Si_2 using high-energy synchrotron X-ray diffraction coupled with Rietveld analysis. The pressurization was achieved using a diamond anvil cell (DAC) which provides quasi-hydrostatic pressures up to 37.6 GPa. Crystal structural variation and equations of state of U_3Si_2 were obtained, and its bulk modulus, *a*- and *c*-axial moduli were derived to be 107.11 ± 5.65 GPa, 82.87 ± 4.78 GPa and 194.52 ± 12.03 GPa, respectively. The determined elastic parameters are compared with those obtained by RUS and nanoindentation.

© 2019 Elsevier B.V. All rights reserved.

1. Introduction

Uranium silicides [1–7] have been considered as alternative fuel materials in Light Water Reactors (LWR) that uses uranium dioxide (UO_2) as the nuclear fuel, and in the generation IV nuclear reactors with enhanced accident tolerance during normal operation or loss-of-coolant events [1]. There are a number of advantageous attributes of U–Si compounds over UO_2, such as higher thermal conductivities at operating temperatures and higher uranium densities (*e.g.* 11.05–14.7 g U cm^{-3} for U-rich U–Si phases) [2–4,6,8]. Among the known U–Si compounds, *e.g.* U_3Si, U_3Si_2, USi and U_3Si_5 [2–4,6,9,10], U_3Si_2 has received major attention due to its relatively high melting point (1938 K) [10], enhanced radiation resistance [11–17], and high thermal stability [7,18], which are favored for nuclear fuel applications. However, there are challenges for utilizing U–Si compounds, as they are generally brittle [5,19,20] and can be susceptible to pulverization under a wide range of conditions relevant to both normal operation and accident environments [6,21–23]. These characteristics make it difficult to directly measure the mechanical properties of U–Si phases at relevant conditions. Nevertheless, in this study, we have obtained improved knowledge of elastic properties of U_3Si_2, which govern mechanical failure processes (*e.g.* material fracturing) and are closely related to the evaluation of thermal stress resistance under various conditions [19,24,25].

U_3Si_2 (space group *P*4/*mbm*) can be treated as a structural

* Corresponding author. Department of Chemistry, Washington State University, Pullman, WA, 99164, United States.
** Corresponding author.
E-mail addresses: x.guo@wsu.edu (X. Guo), hxu@lanl.gov (H. Xu).

https://doi.org/10.1016/j.jnucmat.2019.06.006
0022-3115/© 2019 Elsevier B.V. All rights reserved.

derivative of Cu_3Au (space group *Pm*3 *m*), where U occupies the Cu site and a pair of Si atoms occupy the Au site [26,27] (Fig. 1a). Density Functional Theory (DFT) calculations by Wang et al. [5] show that the bonding features of this intermetallic compound are quite versatile where all three bonding types — ionic, metallic, and covalent bonds — occur via the interactions of U–Si, U–U, and Si–Si, respectively. Such structural characteristics underlie the thermophysical, thermochemical and mechanical properties of U_3Si_2. The temperature-dependent thermal conductivities of U_3Si_2 were studied experimentally up to 1773 K by White et al. [3] and theoretically by Zhang et al. [28]. The thermal oxidation and phase stability were recently assessed by a number of researchers [3,6,21,29–31]. The enthalpy of formation of U_3Si_2 was previously measured by Alcock and Grieveson [32] and Gross et al. [33], and recently re-evaluated to be -33.2 ± 3.1 kJ/mol·atom by Guo et al. [7] using high temperature oxidative drop calorimetry [34–37]. The elastic properties of U_3Si_2 were measured by Carvajal-Nunez et al. [19,20], but there is only a scant dataset including the Young's modulus ($E = 130.4 \pm 0.5$ GPa) and bulk modulus ($K = 68.3 \pm 0.5$ GPa) from resonant ultrasound spectroscopy (RUS) [19], and $E = 153 \pm 2$ GPa from nanoindentation (which also yielded a microhardness of 4.5 GPa) [20]. However, there is a significant difference between the two reported *E* values, and the experimentally determined *E* and *K* values do not agree well with theoretical calculations [5] where *E* and *K* were predicted to be 163.06 GPa and 92.01 GPa, respectively. Therefore, a major objective of this work is to revisit the bulk modulus of U_3Si_2 by performing *in situ* high pressure synchrotron X-ray diffraction (XRD) [38–46]. This method can characterize the intrinsic compressibility of U_3Si_2 through determination of its pressure-dependent structural variation that is not susceptible to its bulk sample properties, such as porosity, grain characteristics, impurity and sample shape, each of which can affect the elastic parameters measured by RUS [19,47].

The combination of high-energy synchrotron XRD with diamond anvil cell (DAC) technique allows for the pressure-dependent structural characterization of U_3Si_2 and an evaluation of its phase equilibrium at high pressures. Such studies have been conducted on two other U–Si compounds, USi and USi_2 [27], but not on U_3Si_2. In addition, pressure is an important variable to tune the physical properties or even generate emergent functionalities of materials through modifying their crystalline/electronic structures and phase stability relations [48–51]. Therefore, our high-pressure synchrotron XRD study of U_3Si_2 will also lay the foundation for future studies on the optimization of material properties of the U–Si system using high pressure processing.

2. Experimental methods

2.1. Sample synthesis and characterization

The starting materials are *1*) U metal containing 31 wppm C impurity with no other impurities detectable by inductively coupled mass spectroscopy; and *2*) silicon powder which is 99.999% pure (Alfa Aesar, USA) without any detectable impurities. U_3Si_2 was synthesized by arc melting of the metallic U and a stoichiometric amount of Si in a tri-arc furnace (Centorr Vacuum Industries, Nashua, NH, USA) using the methods described previously [3]. The phase purity of our synthesized U_3Si_2 sample was confirmed by powder XRD (referenced by ICSD No. 31648, Fig. 1b) using a Bruker D2 Phaser diffractometer (Bruker, Wisconsin, USA) at Los Alamos National Laboratory (LANL) and later at beamline 6-IDD of the Advanced Photon Source (APS), Argonne National Laboratory (ANL). Other complimentary characterization results have been described in a previous publication [7].

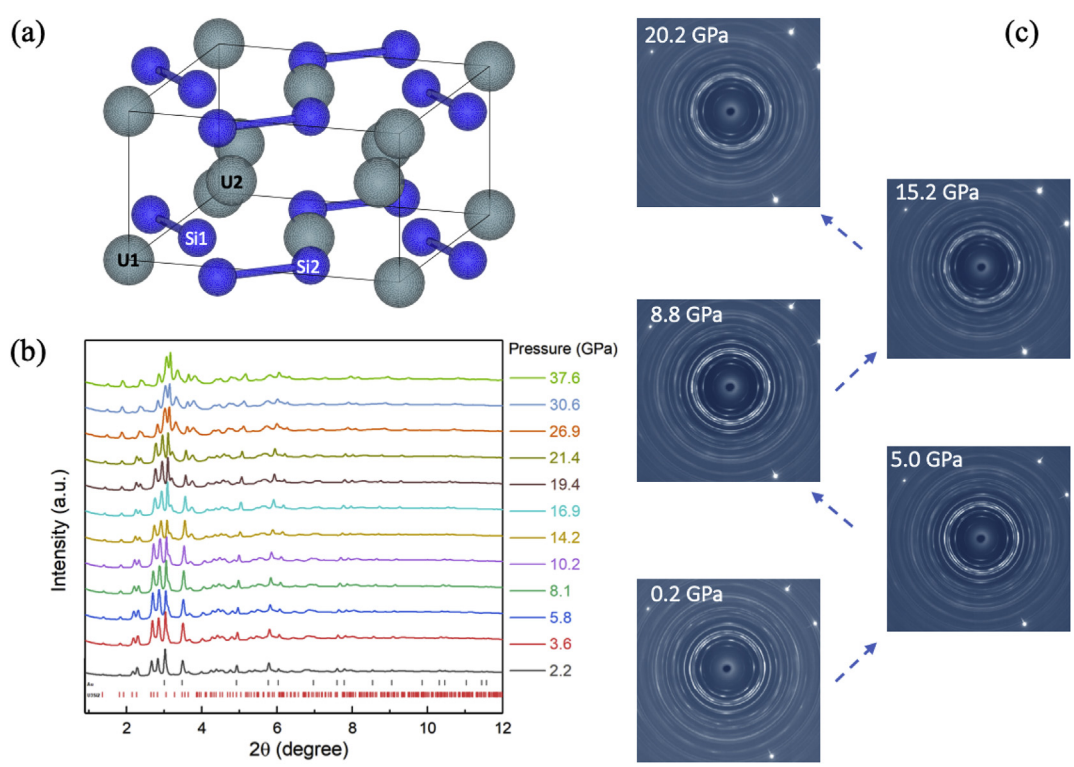

Fig. 1. *In situ* structural characterization of U_3Si_2 under high pressures: (a) crystal structure of U_3Si_2; (b) integrated XRD patterns as a function of pressure up to 37.6 GPa during the decompression; (c) 2D diffraction images at five selected pressure points.

2.2. In situ high-pressure, high-energy synchrotron X-ray diffraction experiments and rietveld analyses

High pressures were generated using a Princeton type symmetric DAC. The sample was loaded in a laser-drilled hole (150 μm diameter) at the center of a pre-indented (40 μm thickness) Inconel gasket, which was encapsulated between two diamonds (culet size 300 μm). Due to the air-sensitivity of U_3Si_2 (it tends to be oxidized in air), the loading was conducted in an Ar-flowing glovebox. A gold wire was placed in the sample compartment as the internal pressure calibrant. A 4:1 methanol:ethanol solution (by volume) was used as the pressure transmitting medium.

The sample-preloaded DAC was double-contained and then transferred to beamline 6-IDD, at APS, ANL, where the *in situ* high-pressure high-energy XRD measurements were conducted. The X-ray wavelength used was 0.123538 Å (100.36 keV), with a beam size of $80 \times 80\ \mu m^2$. Two-dimensional (2D) diffraction images were collected using an amorphous silicon area detector (PerkinElmer XRD 1621), and the geometric parameters were calibrated using a CeO_2 standard. The sample to detector distance was fixed at 502.3 mm. At each pressure point, the sample was exposed to the incident X-rays for 10 s (0.01 s × 1000) to acquire diffraction images with sufficient ring intensities. The obtained 2D diffraction images were corrected for dark current, integrated and calibrated using General Structure Analysis System software version II (GSAS-II) [52] to obtain the patterns that are plotted in intensity as a function of diffraction angle 2θ (Fig. 1b). The diffraction patterns were analyzed by the Rietveld method with GSAS-II, where the instrument parameters were fixed at those obtained from fitting of the diffraction peaks of CeO_2. The background was fitted with the Chebyshev function (10 terms), and the peak profiles with pseudo-Voigt convolution functions [53]. Such procedures were described previously [50,54–58].

The starting structural parameters for refining the structures of U_3Si_2 (ICSD No. 31648), and Au (ICSD No. 52249) under compression were from Zachariasen [59] and Ichikawa [60], and Wyckoff [61], respectively. The final two-phase (U_3Si_2 and Au) structural refinements at all the pressure points achieved convergence, with R_{wp} ranging from 2.9% to 5.5% (Table 1). Representative fitted patterns are shown in Fig. 2. The obtained unit-cell parameters are listed in Table 1. The fitting of the equation of state (EOS) of U_3Si_2 based on its unit-cell parameters at different pressures was performed with the EosFit7 program [62,63].

3. Results and discussion

Due to some relatively large grains (~100 μm) of the U_3Si_2 sample loaded in the DAC, the diffraction images obtained during compression consist of a few sets of single-crystal diffraction spots, which cannot be analyzed as powder XRD data with GSAS-II. However, these large grains were crushed at higher pressures into smaller grains with homogenous distributions in size and orientation, resulting in smooth diffraction rings (Fig. 1c) suitable for Rietveld analysis. Thus, we used the XRD data collected during subsequent decompression to derive structural parameters of U_3Si_2 at various pressures.

Pressures were determined from the derived cell volumes of Au based on its equation of state (EOS) [64] (Fig. 3a). The uncertainties of the determined pressures are due to the propagation of errors associated with Au cell volumes. With increasing pressure, the unit cell of U_3Si_2 contracts continuously (Table 1), as reflected by decreases in its lattice parameters a and c (Fig. 4). Moreover, there is no emergence or disappearance of diffraction peaks on increasing pressure to ~40 GPa, suggesting that U_3Si_2 undergoes no discernible phase transitions. The elastic prosperities of U_3Si_2 can be determined by analyzing the pressure-dependent structural data, especially lattice parameters. The unit cell volume–pressure relation can be fitted by the second order Birch-Murnaghan equation of state [65]:

$$P = \frac{3K_0}{2}\left[\left(\frac{V_0}{V}\right)^{\frac{7}{3}} - \left(\frac{V_0}{V}\right)^{\frac{5}{3}}\right]\left\{1 + \frac{3}{4}\left(K_0' - 4\right)\left[\left(\frac{V_0}{V}\right)^{\frac{2}{3}} - 1\right]\right\} \quad (1)$$

where V_0 is the zero-pressure cell volume, V is the cell volume at a given pressure P, K_0 is bulk modulus, and K_0' is the pressure derivative of K_0, which is fixed at 4 [65]. Least-squares fitting of equation (1) to the experimental P–V data yielded a K_0 of 107.11 ± 5.65 GPa and V_0 of 211.45 ± 1.24 Å^3 (slightly larger than the literature value of 209.59 Å^3 [60]). The derived K_0 value is much larger than that determined by RUS (68.3 GPa) [19], but is in general agreement with the DFT-derived value, 92.01 GPa [5]. The smaller value from RUS is probably a result of sample-dependent bulk characteristics, such as weight, impurity, porosity, and symmetrical shape, which can all contribute to the underestimation [19,47]. On the other hand, the RUS result is of practical interest, as it reflects the engineering modulus of U_3Si_2 materials from scaled-up fabrication whose microstructural defects and compositional variances cannot be effectively eliminated. However, even though the method for obtaining K_0 in this work is immune to deviations caused by sample preparation or bulk defects, its accuracy still depends on the confidence of the determined pressures, the (quasi-)hydrostaticity during compression or decompression, and the quality of the obtained high-pressure XRD data.

Table 1
Unit-cell parameters and refinement agreement indices of U_3Si_2 at high pressures.

Pressure (GPa)	U_3Si_2			Au		
	a (Å)	c (Å)	V (Å^3)	a (Å)	V (Å^3)	R_{wp} (%)
2.2 ± 1.1	7.311(2)	3.883(1)	207.55(9)	4.062(1)	67.00(6)	3.20
3.6 ± 1.1	7.263(3)	3.856(2)	203.41(23)	4.054(1)	66.64(6)	3.18
5.8 ± 1.3	7.231(3)	3.843(2)	200.93(26)	4.042(1)	66.06(7)	2.96
8.1 ± 1.3	7.193(4)	3.829(2)	198.14(26)	4.029(1)	65.40(7)	2.91
10.2 ± 1.3	7.157(4)	3.815(2)	195.40(28)	4.016(2)	64.77(7)	3.05
14.2 ± 1.8	7.088(5)	3.795(3)	190.62(37)	3.992(2)	63.62(10)	3.46
16.9 ± 1.3	7.041(4)	3.778(3)	187.34(26)	3.977(1)	62.89(7)	3.00
19.4 ± 1.5	6.998(4)	3.764(3)	184.32(29)	3.963(2)	62.24(8)	2.90
21.4 ± 1.6	6.967(4)	3.755(3)	182.27(30)	3.953(2)	61.77(9)	2.96
26.9 ± 1.0	6.883(4)	3.737(3)	177.05(21)	3.927(1)	60.55(6)	4.53
30.6 ± 1.0	6.847(3)	3.730(2)	174.91(13)	3.910(2)	59.78(5)	4.80
37.6 ± 1.5	6.735(4)	3.714(3)	168.46(19)	3.881(2)	58.46(8)	5.45

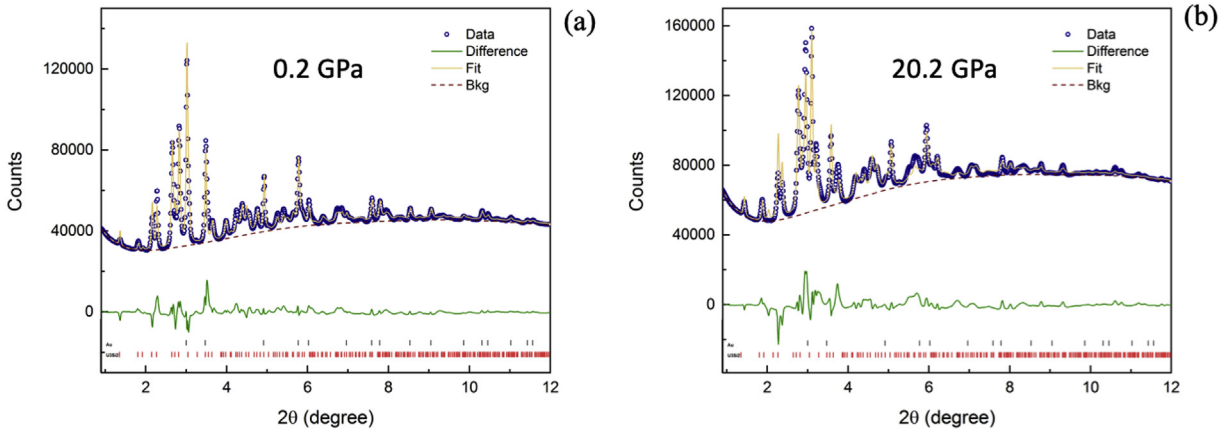

Fig. 2. Representative fitted synchrotron XRD patterns of Au and U_3Si_2 at (a) 0.2 GPa and (b) 20.2 GPa.

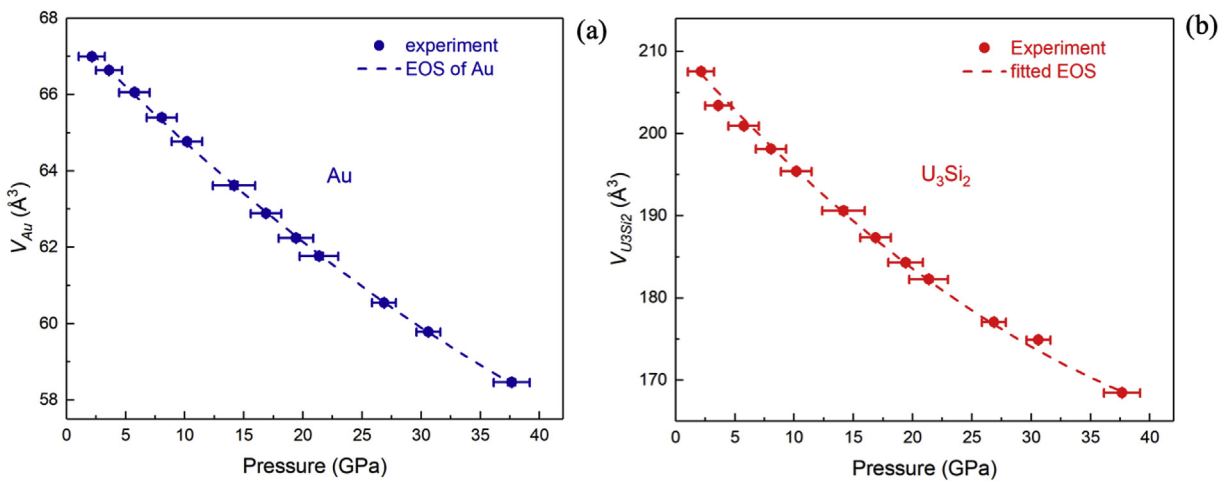

Fig. 3. *P–V* relations of Au and U_3Si_2 using the unit-cell volumes obtained from Rietveld analyses: (a) the pressures determined from the equation of state of Au; (b) the fitted equation of state of U_3Si_2 using the Birch-Murnaghan equation.

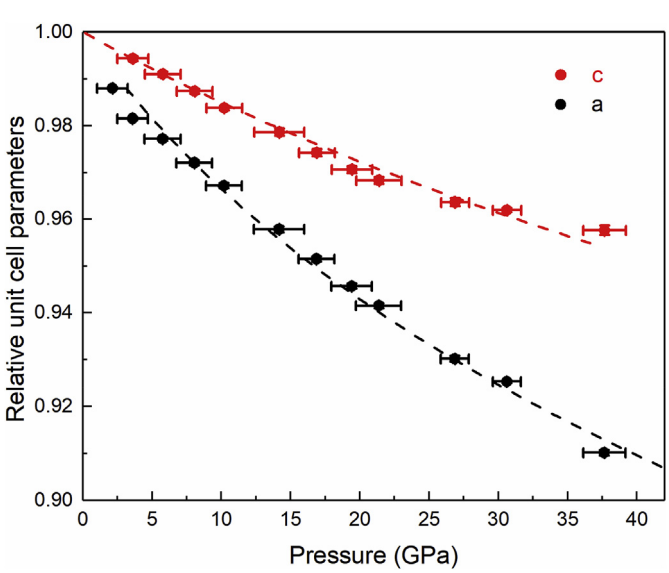

Fig. 4. Variations of the relative unit cell parameters as a function of pressure.

One way to check the quality of the fitted EOS is to compare the derived bulk modulus with that obtained by linear moduli through the relation [62] $K_{0,lm} = 3\cdot\left(\frac{1}{M_{a,0}}+\frac{1}{M_{a,0}}+\frac{1}{M_{c,0}}\right)^{-1}$, where $M_{a,0}$ and $M_{c,0}$ are the linear moduli along the *a*- and *c*-axis, respectively, which define the linear compressibility at zero pressure. Similar to the volume–pressure relation, variations of unit cell parameters with pressure can be fitted to the one-dimensional analog of the Birch-Murnaghan equation of state [39] (Fig. 4) by replacing *V* in equation (1) with a^3 or c^3:

$$P=\frac{3M_{a,0}}{2}\left[\left(\frac{a_0}{a}\right)^7-\left(\frac{a_0}{a}\right)^5\right], P=\frac{3M_{c,0}}{2}\left[\left(\frac{c_0}{c}\right)^7-\left(\frac{c_0}{c}\right)^5\right], \quad (2)$$

where a_0 and c_0 are unit-cell parameters at zero pressure. The linear moduli can then be derived from the fitted curves of *a* and *c* as a function of pressure to be $M_{a,0} = 82.87 \pm 4.78$ GPa and $M_{c,0} = 194.52 \pm 12.03$ GPa. The $K_{0,lm}$ obtained from linear moduli is 102.48 GPa, which is in good agreement with the directly derived K_0, 107.11 GPa. Note that the linear modulus along the *c*-axis is ~2.4 times that along the *a*-axis, suggesting that the structure is less compressible along the *c*-axis. Such anisotropic compressibility is evident in Fig. 4, where the rate of contraction in the relative *c* value is smaller than that in *a*, with a decelerating trend at higher pressures.

The anisotropic behavior in axial compressibility can be explained by the susceptibility of various bond distances to compression (Fig. 5). The unit-cell parameters and atomic coordinates of U_3Si_2 at various pressures are listed in Tables 1 and 2, respectively, from which the evolution of bond lengths as a function of pressure can be obtained. At the lowest pressure measured, 2.2 GPa, the structure of U_3Si_2 is close to that under the ambient condition (1 atm). There are two types of U atoms situating within two layers parallel to (001) in a unit cell (Fig. 1a). In the (001) layer, each U1 atom is coordinated to four in-plane Si atoms as the nearest

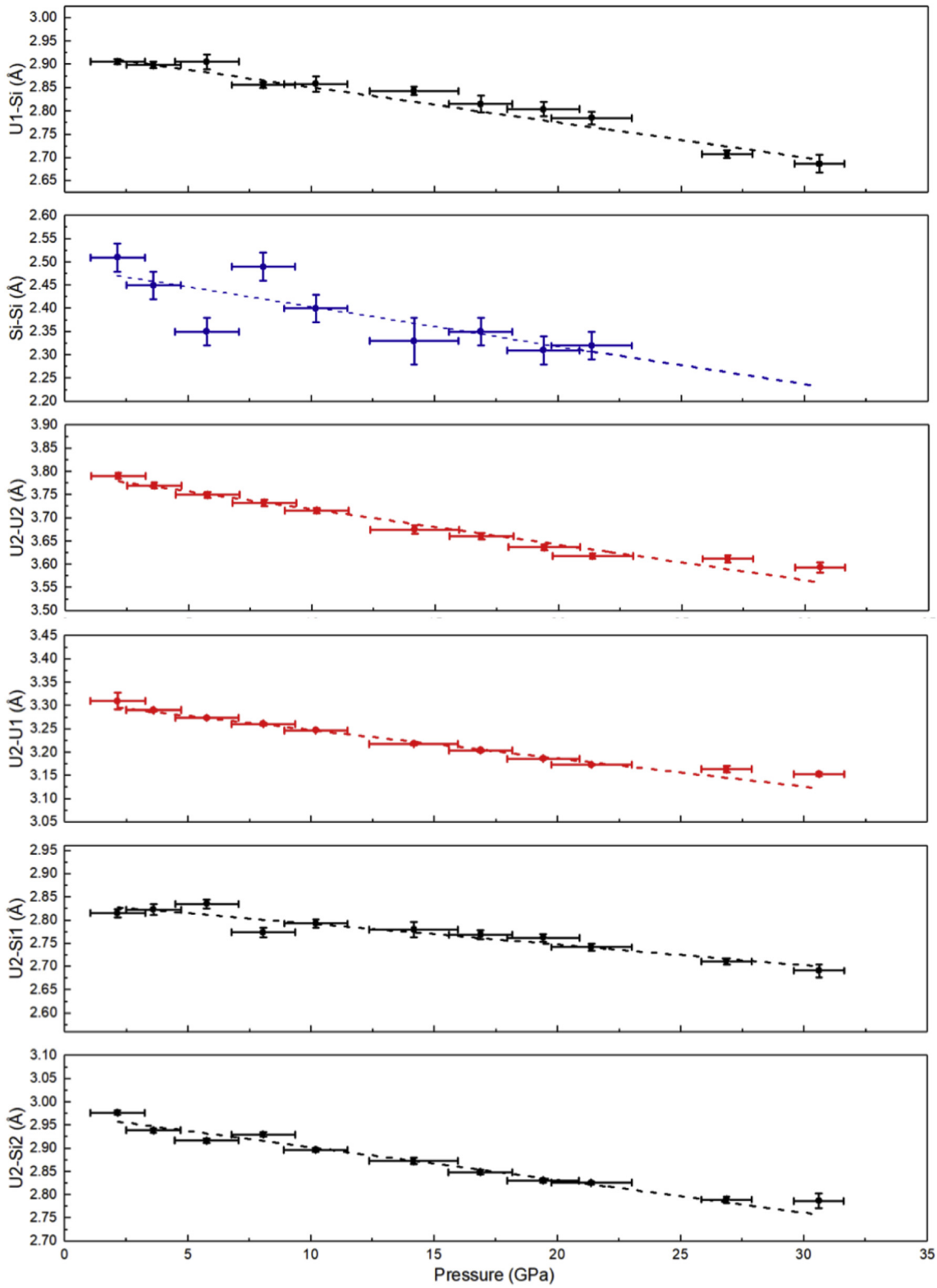

Fig. 5. Variations of bond lengths as a function of pressure.

Table 2
Atomic coordinates and atomic displacement parameters of U_3Si_2 at high pressures.

Pressure (GPa)	U1(*x*, *y*, 0.5)		Si(*x*, *y*, 0.0)				
	x	*y*	*x*	*y*	U_{iso}(U1) (Å^2/100)	U_{iso}(U2) (Å^2/100)	U_{iso}(Si) (Å^2/100)
2.2 ± 1.1	0.1803(5)	0.6803(5)	0.6249(26)	0.1249(26)	0.1(2)	3.5(3)	3.8(6)
3.6 ± 1.1	0.1802(6)	0.6802(6)	0.6191(29)	0.1191(29)	0.0(2)	6.2(5)	3.8(6)
5.8 ± 1.3	0.1805(5)	0.6805(5)	0.6198(26)	0.1198(26)	0.2(1)	9.0(6)	4.5(7)
8.1 ± 1.3	0.1786(7)	0.6786(7)	0.6253(11)	0.1156(27)	0.2(1)	9.8(5)	2.6(11)
10.2 ± 1.3	0.1800(6)	0.6800(6)	0.6195(25)	0.1195(25)	0.0(1)	8.9(5)	1.8(6)
14.2 ± 1.8	0.1806(10)	0.6806(10)	0.6166(36)	0.1166(36)	0.3(1)	8.9(11)	2.2(14)
16.9 ± 1.3	0.1770(6)	0.6770(6)	0.6279(29)	0.1279(29)	0.1(1)	8.1(6)	2.6(7)
19.4 ± 1.5	0.1775(5)	0.6775(5)	0.6287(26)	0.1287(26)	0.1(1)	8.1(5)	2.6(7)
21.4 ± 1.6	0.1774(5)	0.6774(5)	0.6291(26)	0.1291(26)	0.1(1)	8.1(6)	2.6(8)
26.9 ± 1.0	0.1741(10)	0.6741(10)	0.6282(56)	0.1286(56)	0.9(1)	8.5(15)	2.6(14)
30.6 ± 1.0	0.1712(11)	0.6712(11)	0.6319(53)	0.1312(53)	1.5(2)	9.4(11)	7.0(22)

neighbors (U1–Si = 2.906(6) Å), and the bond distance between the two Si atoms of a covalent Si–Si pair (Si–Si) is 2.51(3) Å. In the (002) layer, each U2 is surrounded by five other in-plane U2 atoms (U2–U2 = 3.791(6) Å), and bonded to six Si atoms (two Si1 and four Si2 atoms) from neighboring (001) layers with a bond distance of U2–Si = 2.815(9) Å or 2.977(5) Å. These bonding parameters are in accordance with experimental [59] and theoretical [5] values. With increasing pressure, the in-plane bonds that is perpendicular to the *c*-axis behave differently from those out-plane bonds parallel to the *c*-axis. As seen from Fig. 5, all the three in-plane bonds U1–Si, Si–Si, and U2–U2 exhibit larger changes upon compression; compared to their values at 2 GPa, they contract by 6%–11% at 30 GPa. On the other hand, the bond interactions along the *c*-axis are more resistant to compression, as reflected by the relatively small changes in the projected distances of diagonal bonding interactions (U2 and other atoms) along the *c*-axis; these interatomic distances contract only by 4%–7% when pressure increases from 2 GPa to 30 GPa. Thus, the anisotropic behavior of interatomic interactions in U_3Si_2 results in the anisotropy in its axial compressibility.

Furthermore, we derived other elastic properties of U_3Si_2. The shear modulus *G* characterizes the resistance of a material to plastic deformation, which cannot be determined directly here. Thus, we used DFT-calculated value $G = 67.68$ GPa [5] in the following derivation. The K/G ratio defines whether a material is ductile or brittle. When $K/G < 1.75$, the material is considered to be brittle, and when $K/G > 1.75$, it is ductile [66]. The zero-pressure K_0/G of U_3Si_2 was determined to be 1.58, which is in general agreement with 1.36 from DFT calculations [5] but significantly larger than 1.24 measured by RUS measurements [19]. Thus, U_3Si_2 at ambient condition is brittle by the above definition, consistent with the experimental observation [67] and theoretical prediction [5]. Lastly, the Young's Modulus *E* and Poisson's ratio υ at ambient condition were evaluated with an isotropic approximation via the following equations (2) and (3) to be 167.72 GPa and 0.24, respectively:

$$E = \frac{9GK_0}{G + 3K_0} \tag{3}$$

$$\upsilon = \frac{3K_0 - 2G}{2(G + 3K_0)} \tag{4}$$

The *E* value from this work is in excellent agreement with that calculated from DFT, 163.06 GPa [5], which is closer to 153 GPa (nanoindentation) [20], but larger than 130.4 GPa (RUS) [19] by ~27%. Poisson's ratio υ, which describes the extent of transverse strains over longitudinal strains, reflects the packing density of atoms and thus is intimately connected to their bonding characteristics [68,69]. Ionic bonds usually provide more dense packing that results in higher values of υ (~0.25), whereas covalent solids with less dense packing have lower values of υ (~0.1) [68,70]. Therefore, both our DAC and previous DFT studies suggest that the U_3Si_2 structure is dominated by ionic contributions from three different U–Si bonds, which is consistent with the brittle nature ($K/G = 1.58$) of U_3Si_2 [69]. The elastic constants derived from this work, previous RUS and nanoindentation measurements are is summarized in Table 3. An important implication from this comparison is the effects of microstructures on the elastic moduli, where the same U_3Si_2 sample was probed at multiple length scales – DAC (atomic), nanoindentation (nano/micro), and RUS (macro). Despite the intrinsic bulk modulus is solely related to bond strength and lattice strain, its macroscale counterpart, the mechanical performance of real-world materials with extrinsic contributions from porosities, defects and impurities etc. can be substantially weakened when the same material is economically scaled up to industrial scales where material properties at macroscale are more relevant because of uncontrolled microstructural imperfections.

Table 3
Elastic properties of U_3Si_2 determined by high-pressure synchrotron XRD, as compared with those calculated from DFT, and derived from RUS and nanoindentation.

	DFT [5]	RUS [19]	Nano-indentation [20]	DAC (this work)
K (GPa)	92.01	68.3 ± 0.3		107.11 ± 5.65
G (GPa)	67.68	55.2 ± 0.5	61.6[b]	
E (GPa)	163.06	130.4 ± 0.5	153.0 ± 2.5	167.7[a]
K/*G*	1.36	1.24	1.74[b]	1.58[a]
υ	0.20	0.182	0.26[b]	0.24[a]

[a] Derived based on $G = 67.68$ GPa from DFT calculation [5].
[b] Calculated based on $K = 107.11$ GPa from this study.

4. Conclusions

In this work, we performed the first static compression/decompression experiments on U_3Si_2 up to 37.6 GPa and characterized its pressure-dependent structural variations using *in situ* diamond-anvil cell, high-energy angle-dispersive X-ray diffraction. The bulk modulus of U_3Si_2 was obtained by fitting the Birch-Murnaghan equation of state to the experimentally obtained *P*–*V* data, to be 107.11 ± 5.65 GPa, which can be used as a benchmark value for future theoretical calculations. Other elastic properties were also evaluated and were found to be consistent with DFT predictions and nanoindentation results, though in poor agreement with RUS-derived values. Future RUS work on single crystals of U_3Si_2 is undergoing to validate the data obtained from this work.

Acknowledgements

Research presented in this article was supported by the

Laboratory Directed Research and Development (LDRD) program of Los Alamos National Laboratory (LANL) under project number 20180007 DR. X.G. acknowledges the support through a LANL Seaborg postdoctoral fellowship and, later, the institutional funds from the Department of Chemistry at Washington State University. LANL, an affirmative action/equal opportunity employer, is managed by Triad National Security, LLC, for the National Nuclear Security Administration of the U.S. Department of Energy under contract 89233218CNA000001. This research used resources of the Advanced Photon Source, a U.S. Department of Energy (DOE) Office of Science User Facility operated for the DOE Office of Science by Argonne National Laboratory under Contract No. DE-AC02-06CH11357.

References

[1] A. Nelson, J. White, D. Byler, J. Dunwoody, J. Valdez, K. McClellan, Overview of properties and performance of uranium-silicide compounds for light water reactor applications, Trans. Am. Nucl. Soc. 110 (2014) 987–989.
[2] J.T. White, A.T. Nelson, D.D. Byler, D.J. Safarik, J.T. Dunwoody, K.J. McClellan, Thermophysical properties of U_3Si_5 to 1773 K, J. Nucl. Mater. 456 (2015) 442–448.
[3] J.T. White, A.T. Nelson, J.T. Dunwoody, D.D. Byler, D.J. Safarik, K.J. McClellan, Thermophysical properties of U_3Si_2 to 1773 K, J. Nucl. Mater. 464 (2015) 275–280.
[4] J.T. White, A.T. Nelson, J.T. Dunwoody, D.D. Byler, K.J. McClellan, Thermophysical properties of USi to 1673 K, J. Nucl. Mater. 471 (2016) 129–135.
[5] T. Wang, N. Qiu, X. Wen, Y. Tian, J. He, K. Luo, X. Zha, Y. Zhou, Q. Huang, J. Lang, First-principles investigations on the electronic structures of U_3Si_2, J. Nucl. Mater. 469 (2016) 194–199.
[6] E.S. Wood, J.T. White, A.T. Nelson, Oxidation behavior of U-Si compounds in air from 25 to 1000 °C, J. Nucl. Mater. 484 (2017) 245–257.
[7] X. Guo, J.T. White, A.T. Nelson, A. Migdisov, R. Roback, H. Xu, Enthalpy of formation of U_3Si_2: a high-temperature drop calorimetry study, J. Nucl. Mater. 507 (2018) 44–49.
[8] T. Le Bihan, H. Noël, P. Rogl, Crystal structure of the uranium monosilicide USi, J. Alloy, Compd 240 (1–2) (1996) 128–133.
[9] J.T. White, A.T. Nelson, D.D. Byler, J.A. Valdez, K.J. McClellan, Thermophysical properties of U_3Si to 1150 K, J. Nucl. Mater. 452 (1–3) (2014) 304–310.
[10] S.C. Middleburgh, R.W. Grimes, E.J. Lahoda, C.R. Stanek, D.A. Andersson, Non-stoichiometry in U_3Si_2, J. Nucl. Mater. 482 (2016) 300–305.
[11] R.C. Birtcher, J.W. Richardson, M.H. Mueller, Amorphization of U_3Si_2 by ion or neutron irradiation, J. Nucl. Mater. 230 (2) (1996) 158–163.
[12] M.R. Finlay, G.L. Hofman, J.L. Snelgrove, Irradiation behaviour of uranium silicide compounds, J. Nucl. Mater. 325 (2–3) (2004) 118–128.
[13] S.J. Zinkle, K.A. Terrani, J.C. Gehin, L.J. Ott, L.L. Snead, Accident tolerant fuels for LWRs: a perspective, J. Nucl. Mater. 448 (1–3) (2014) 374–379.
[14] Y.B. Miao, J. Harp, K. Mo, S. Bhattacharya, P. Baldo, A.M. Yacout, Short Communication on "In-situ TEM ion irradiation investigations on U_3Si_2 at LWR temperatures, J. Nucl. Mater. 484 (2017) 168–173.
[15] Y. Miao, J. Harp, K. Mo, Y.S. Kim, S. Zhu, A.M. Yacout, Microstructure investigations of U_3Si_2 implanted by high-energy Xe ions at 600 °C, J. Nucl. Mater. 503 (2018) 314–322.
[16] T. Yao, B. Gong, L. He, Y. Miao, J.M. Harp, M. Tonks, J. Lian, In-situ TEM study of the ion irradiation behavior of U_3Si_2 and U_3Si_5, J. Nucl. Mater. 511 (2018) 56–63.
[17] T. Yao, B. Gong, L. He, J. Harp, M. Tonks, J. Lian, Radiation-induced grain subdivision and bubble formation in U_3Si_2 at LWR temperature, J. Nucl. Mater. 498 (2018) 169–175.
[18] A. Berche, C. Rado, O. Rapaud, C. Gueneau, J. Rogez, Thermodynamic study of the U-Si system, J. Nucl. Mater. 389 (1) (2009) 101–107.
[19] U. Carvajal-Nunez, T.A. Saleh, J.T. White, B. Maiorov, A.T. Nelson, Determination of elastic properties of polycrystalline U_3Si_2 using resonant ultrasound spectroscopy, J. Nucl. Mater. 498 (2018) 438–444.
[20] U. Carvajal-Nunez, M. Elbakhshwan, N. Mara, J. White, A. Nelson, Mechanical properties of uranium silicides by nanoindentation and finite elements modeling, JOM-US 70 (2) (2018) 203–208.
[21] E.S. Wood, J.T. White, A.T. Nelson, The effect of aluminum additions on the oxidation resistance of U_3Si_2, J. Nucl. Mater. 489 (2017) 84–90.
[22] E.S. Wood, J.T. White, C.J. Grote, A.T. Nelson, U_3Si_2 behavior in H_2O: Part I, flowing steam and the effect of hydrogen, J. Nucl. Mater. 501 (2018) 404–412.
[23] A.T. Nelson, A. Migdisov, E.S. Wood, C.J. Grote, U_3Si_2 behavior in H_2O environments: Part II, pressurized water with controlled redox chemistry, J. Nucl. Mater. 500 (2018) 81–91.
[24] C. Smith, Thermal stresses and their significance in nuclear fuel elements, J. Am. Soc. Nav. Eng. 72 (3) (1960) 393–400.
[25] H. Matzke, Indentation Fracture and Mechanical Properties of Ceramic Fuels and Glasses, Applied Research Resport, Harwood, 1987.
[26] P. Villars, L. Calvert, 's Pearson, Handbook of Crystallographic Data for Intermetallic Compounds, second ed., American Society of Metals, Cleveland, OH, 1991.
[27] S. Yagoubi, S. Heathman, A. Svane, G. Vaitheeswaran, P. Heines, J.-C. Griveau, T. Le Bihan, M. Idiri, F. Wastin, R. Caciuffo, High pressure studies on uranium and thorium silicide compounds: experiment and theory, J. Alloy. Comp. 546 (2013) 63–71.
[28] Y. Zhang, A.D.R. Andersson, A Thermal Conductivity Model for U-Si Compounds, Los Alamos National Laboratory, Los Alamos, 2017.
[29] K. Johnson, V. Strom, J. Wallenius, D.A. Lopes, Oxidation of accident tolerant fuel candidates, J. Nucl. Sci. Technol. 54 (3) (2017) 280–286.
[30] E. Jossou, U. Eduok, N.Y. Dzade, B. Szpunar, J.A. Szpunar, Oxidation behaviour of U_3Si_2: an experimental and first principles investigation, Phys. Chem. Chem. Phys. 20 (7) (2018) 4708–4720.
[31] C.-K. Chung, X. Guo, G. Wang, J.T. White, A.T. Nelson, A. Shelyug, H. Boukhalfa, P. Yang, E.R. Batista, A.A. Migdissov, R.C. Roback, A. Navrotsky, H. Xu, Enthalpies of formation and phase stability relations of USi, U_3Si_5 and U_3Si_2, J. Nucl. Mater. 523 (2019) 101–110.
[32] C.B. Alcock, P. Grieveson, Thermodynamic study of compounds of uranium with silicon, germanium, tin, and lead, J. Inst. Met. 90 (8) (1962) 304.
[33] P. Gross, C. Hayman, H. Clayton, Heats of Formation of Uranium Silicides and Nitrides, Thermodynamics of Nuclear Materials, International Atomic Energy Agency, Vienna, 1962, pp. 653–665.
[34] A. Navrotsky, Progress and new directions in calorimetry: a 2014 perspective, J. Am. Ceram. Soc. 97 (11) (2014) 3349–3359.
[35] X. Guo, A. Navrotsky, R.K. Kukkadapu, M.H. Engelhard, A. Lanzirotti, M. Newville, E.S. Ilton, S. Sutton, H. Xu, Structure and thermodynamics of uranium containing iron garnets Geochim, Cosmochim. Acta 189 (2016) 269–281.
[36] X. Guo, S. Szenknect, A. Mesbah, N. Clavier, C. Poinssot, D. Wu, H. Xu, N. Dacheux, R.C. Ewing, A. Navrotsky, Energetics of a uranothorite (Th1-*x*U*x*SiO4) solid solution, Chem. Mater. 28 (19) (2016) 7117–7124.
[37] X. Guo, H. Boukhalfa, J.N. Mitchell, M. Ramos, A.J. Gaunt, A. Migliori, R. Roback, A. Navrotsky, H. Xu, Sample seal-and-drop device for drop calorimetry and its application to high temperature oxide melt drop solution measurements of PuO_2, Rev. Sci. Instrum. 90 (4) (2019), 044101.
[38] J. Zhang, A. Celestian, J.B. Parise, H. Xu, P.J. Heaney, A new polymorph of eucryptite ($LiAlSiO_4$), ε-eucryptite, and thermal expansion of α-and ε-eucryptite at high pressure, Am. Mineral. 87 (4) (2002) 566–571.
[39] H. Xu, Y. Zhao, J. Zhang, D.D. Hickmott, L.L. Daemen, In situ neutron diffraction study of deuterated portlandite $Ca(OD)_2$ at high pressure and temperature, Phys. Chem. Miner. 34 (4) (2007) 223–232.
[40] H. Xu, J. Zhang, Y. Zhao, G.D. Guthrie, D.D. Hickmott, A. Navrotsky, Compressibility and pressure-induced amorphization of guest-free melanophlogite: an in-situ synchrotron X-ray diffraction study, Am. Mineral. 92 (1) (2007) 166–173.
[41] Y. Wang, J. Zhang, H. Xu, Z. Lin, L.L. Daemen, Y. Zhao, L. Wang, Thermal equation of state of copper studied by high P-T synchrotron X-ray diffraction, Appl. Phys. Lett. 94 (7) (2009), 071904.
[42] H. Xu, Y. Zhao, J. Zhang, Y. Wang, D.D. Hickmott, L.L. Daemen, M.A. Hartl, L. Wang, Anisotropic elasticity of jarosite: a high-P synchrotron XRD study, Am. Mineral. 95 (1) (2010) 19–23.
[43] J. Zhu, H. Xu, J. Zhang, C. Jin, L. Wang, Y. Zhao, Thermal equations of state and phase relation of $PbTiO_3$: a high PT synchrotron X-ray diffraction study, J. Appl. Phys. 110 (8) (2011), 084103.
[44] Z. Quan, Z. Luo, Y. Wang, H. Xu, C. Wang, Z. Wang, J. Fang, Pressure-induced switching between amorphization and crystallization in PbTe nanoparticles, Nano Lett. 13 (8) (2013) 3729–3735.
[45] S. Wang, X. Yu, J. Zhang, Y. Zhang, L. Wang, K. Leinenweber, H. Xu, D. Popov, C. Park, W. Yang, Crystal structures, elastic properties, and hardness of high-pressure synthesized CrB_2 and CrB_4, J. Superhard Mater. 36 (4) (2014) 279–287.
[46] J. Zhu, J. Zhang, H. Xu, S.C. Vogel, C. Jin, J. Frantti, Y. Zhao, Pressure-induced reversal between thermal contraction and expansion in ferroelectric $PbTiO_3$, Sci. Rep. 4 (2014) 3700.
[47] A. Migliori, J.L. Sarrao, Resonant Ultrasound Spectroscopy: Applications to Physics, Materials Measurements, and Nondestructive Evaluation, Wiley, New York, 1997.
[48] J. Zhu, S. Du, X. Yu, J. Zhang, H. Xu, S.C. Vogel, T.C. Germann, J.S. Francisco, F. Izumi, K. Momma, Y. Kawamura, C. Jin, Y. Zhao, Encapsulation kinetics and dynamics of carbon monoxide in clathrate hydrate, Nat. Commun. 5 (2014) 4128.
[49] T. Wang, R. Li, Z. Quan, W.S. Loc, W.A. Bassett, H. Xu, Y.C. Cao, J. Fang, Z. Wang, Pressure processing of nanocube assemblies toward harvesting of a metastable PbS phase, Adv. Mater. 27 (31) (2015) 4544–4549.
[50] X. Lü, Y. Wang, C.C. Stoumpos, Q. Hu, X. Guo, H. Chen, L. Yang, J.S. Smith, W. Yang, Y. Zhao, H. Xu, M.G. Kanatzidis, Q. Jia, Enhanced structural stability and photo responsiveness of $CH_3NH_3SnI_3$ perovskite via pressure-induced amorphization and recrystallization, Adv. Mater. 28 (39) (2016) 8663–8668.
[51] G. Bounos, M. Karnachoriti, A.G. Kontos, C.C. Stoumpos, L. Tsetseris, A. Kaltzoglou, X. Guo, X. Lü, Y.S. Raptis, M.G. Kanatzidis, Defect perovskites under pressure: structural evolution of Cs_2SnX_6 (X= Cl, Br, I), J. Phys. Chem. C 122 (42) (2018) 24004–24013.
[52] B.H. Toby, R.B. Von Dreele, GSAS-II: the genesis of a modern open-source all purpose crystallography software package, J. Appl. Crystallogr. 46 (2) (2013) 544–549.
[53] P. Thompson, D. Cox, J. Hastings, Rietveld refinement of Debye–Scherrer

synchrotron X-ray data from Al_2O_3, J. Appl. Crystallogr. 20 (2) (1987) 79–83.
[54] M.L. Balmer, Y. Su, H. Xu, E. Bitten, D. McCready, A. Navrotsky, Synthesis, structure determination, and aqueous durability of $Cs_2ZrSi_3O_9$, J. Am. Ceram. Soc. 84 (1) (2001) 153–160.
[55] H. Xu, A. Navrotsky, M.L. Balmer, Y. Su, Crystal chemistry and phase transitions in substituted pollucites along the $CsAlSi_2O_6$-$CsTiSi_2O_{6.5}$ join: a powder synchrotron X-ray diffractometry study, J. Am. Ceram. Soc. 85 (5) (2002) 1235–1242.
[56] H. Xu, Y. Zhao, S.C. Vogel, L.L. Daemen, D.D. Hickmott, Anisotropic thermal expansion and hydrogen bonding behavior of portlandite: a high-temperature neutron diffraction study, J. Solid State Chem. 180 (4) (2007) 1519–1525.
[57] H. Xu, M.E. Chavez, J.N. Mitchell, T.J. Garino, H.L. Schwarz, M.A. Rodriguez, D.X. Rademacher, T.M. Nenoff, Crystal structure and thermodynamic stability of Ba/Ti-substituted pollucites for radioactive Cs/Ba immobilization, J. Am. Ceram. Soc. 98 (8) (2015) 2634–2640.
[58] H. Xu, X. Guo, J. Bai, Thermal behavior of polyhalite: a high-temperature synchrotron XRD study, Phys. Chem. Miner. 44 (2) (2017) 125–135.
[59] W. Zachariasen, Crystal chemical studies of the 5*f*-series of elements. VIII. Crystal structure studies of uranium silicides and of $CeSi_2$, $NpSi_2$, and $PuSi_2$, Acta Crystallogr. 2 (2) (1949) 94–99.
[60] R.U. Ichikawa, R.H. Garcia, A.S.d. Silva, X. Turrillas, A.M. Saliba-Silva, N.B. Lima, L.G. Martinez, Structural and Microstructural Characterization of U_3Si_2 Nuclear Fuel Using X-Ray Diffraction, International Nuclear Altantic Conference - INAC 2017, ASSOCIAÇÃO BRASILEIRA DE ENERGIA NUCLEAR – ABEN, Belo Horizonte, MG, Brazil, 2017.
[61] R.W. Wyckoff, Crystal Structures, vol. 1, Interscience Publ., 1971.
[62] R.J. Angel, M. Alvaro, J. Gonzalez-Platas, EosFit7c and a Fortran module (library) for equation of state calculations, Z. für Kristallogr. - Cryst. Mater. 229 (5) (2014) 405–419.
[63] J. Gonzalez-Platas, M. Alvaro, F. Nestola, R. Angel, EosFit7-GUI: a new graphical user interface for equation of state calculations, analyses and teaching, J. Appl. Crystallogr. 49 (4) (2016) 1377–1382.
[64] D.L. Heinz, R. Jeanloz, The equation of state of the gold calibration standard, J. Appl. Phys. 55 (4) (1984) 885–893.
[65] F. Birch, Finite elastic strain of cubic crystals, Phys. Rev. 71 (11) (1947) 809.
[66] S. Pugh, XCII. Relations between the elastic moduli and the plastic properties of polycrystalline pure metals, Lond. Edinb. Dubl. Phil. Mag. 45 (367) (1954) 823–843.
[67] A. Dwight, Study of the Uranium-Aluminum-Silicon System, Argonne National Lab., IL (USA), 1982.
[68] W. Köster, H. Franz, Poisson's ratio for metals and alloys, Metall. Rev. 6 (1) (1961) 1–56.
[69] G.N. Greaves, A.L. Greer, R.S. Lakes, T. Rouxel, Poisson's ratio and modern materials, Nat. Mater. 10 (2011) 823–837.
[70] J. Yang, J. Long, L. Yang, D. Li, First-principles investigations of the physical properties of binary uranium silicide alloys, J. Nucl. Mater. 443 (1–3) (2013) 195–199.